Multifunctional role of GPCR signaling in epithelial tube formation

Vishakha Vishwakarma, Thao Phuong Le, and SeYeon Chung*

Department of Biological Sciences, Louisiana State University, Baton Rouge, LA 70803, USA

*Author for correspondence: seyeonchung@lsu.edu

Key words: *Drosophila*, Salivary gland, Fog signaling, GPCR, Actomyosin

Running title: GPCR signaling in tube formation

ABSTRACT

Epithelial tube formation requires Rho1-dependent actomyosin contractility to generate the cellular forces that drive cell shape changes and rearrangement. Rho1 signaling is activated by G protein-coupled receptor (GPCR) signaling at the cell surface. During *Drosophila* embryonic salivary gland (SG) invagination, the GPCR ligand Folded gastrulation (Fog) activates Rho1 signaling to drive apical constriction. The SG receptor that transduces the Fog signal into Rho1-dependent myosin activation has not been identified. Here, we reveal that the Smog GPCR transduces Fog signal to regulate Rho kinase accumulation and myosin activation in the medioapical region of cells to control apical constriction during SG invagination. We also report on unexpected Fog-independent roles for Smog in maintaining epithelial integrity and organizing cortical actin. Our data supports a model wherein Smog regulates distinct myosin pools and actin cytoskeleton in a ligand-dependent manner during epithelial tube formation.

INTRODUCTION

The formation of three-dimensional tubes by invagination from flat epithelial sheets is a fundamental process in forming organs, such as lungs and kidneys (Andrew and Ewald, 2010). The *Drosophila* embryonic salivary gland (SG) is a premier model system to study the mechanisms underlying epithelial tube morphogenesis (Chung et al., 2014; Girdler and Röper, 2014). The SG begins as a two-dimensional plate of cells on the embryo surface. Neither cell division nor cell death occurs once the SG cells are specified; all the morphogenetic changes arise by changes in cell shape and rearrangement.

A major cell shape change during SG invagination is apical constriction, wherein the apical side of epithelial cells shrinks while keeping the nearly constant volume (Lubarsky and Krasnow, 2003; Martin and Goldstein, 2014). During stage 11, SG cells begin to invaginate at the dorsal/posterior region of the placode through apical constriction (Fig. 1A). This leads to forming a narrow invagination pit through which all SG cells eventually internalize. Apical constriction is observed in both invertebrates and vertebrates, driving morphogenetic processes ranging from gastrulation in *Drosophila* and *Xenopus* to lens formation in the mouse eye to formation of tubular organs such as the *Drosophila* SG and chicken lungs (Kim et al., 2013; Myat and Andrew, 2000; Plageman et al., 2011; Sweeton et al., 1991). Defects in apical constriction result in defects in overall tissue shape, suggesting that coordinated apical constriction is required for final tissue architecture (Chung et al., 2017; Guglielmi et al., 2015; Izquierdo et al., 2018).

Contractile actomyosin networks generate the cellular forces driving coordinated cell behaviors during epithelial morphogenesis (Gorfinkiel and Blanchard, 2011; Levayer and Lecuit, 2012; Munjal and Lecuit, 2014). Non-muscle myosin II (hereafter referred to as myosin) uses its motor activity to pull on actin filaments anchored to adherens junctions (AJs) to apply tension on the junction and neighboring cells. Three distinct pools of myosin generate the contractile forces required for SG invagination (Booth et al., 2014; Chung et al., 2017; Röper, 2012). Medioapical myosin forms in the center of the apical side of the SG cell and drives apical constriction (Booth et al., 2014; Chung et

al., 2017; Röper, 2012). Junctional myosin, associated with AJs of SG cells, is involved in cell intercalation (Sanchez-Corrales et al., 2018). A supracellular myosin cable surrounding the entire SG placode generates the tissue-level compressing force (Chung et al., 2017; Röper, 2012). From studies in the past several years by us and others, we are beginning to understand how each myosin pool is created and regulated during SG invagination (Booth et al., 2014; Chung et al., 2017; Le and Chung, 2021; Röper, 2012; Sanchez-Corrales et al., 2018; Sidor et al., 2020).

Localized activation of the RhoA (Rho1 in *Drosophila*) GTPase is key to creating and/or polarizing contractile myosin structures in epithelial cells (Blanchard et al., 2010; Dawes-Hoang et al., 2005; Martin et al., 2009; Mason et al., 2013). Studies in *Drosophila* have identified the Folded gastrulation (Fog) pathway as a key signaling pathway regulating Rho1 signaling during epithelial morphogenesis (Manning and Rogers, 2014). During *Drosophila* gastrulation, two G protein-coupled receptors (GPCRs), Smog (ubiquitously expressed) and Mist (mesoderm-specific), respond to Fog to activate heterotrimeric G proteins, Rho1, and Rho kinase (Rok) to regulate myosin contractility (Costa et al., 1994; Dawes-Hoang et al., 2005; Kerridge et al., 2016; Kölsch et al., 2007; Manning et al., 2013; Mason et al., 2013; Parks and Wieschaus, 1991). In our previous study in the SG, we also revealed a tissue-specific regulation of Fog signaling to activate myosin contractility: the Fork head (Fkh) transcription factor regulates SG upregulation of *fog*, which promotes accumulation of Rok and myosin specifically in the medioapical region of SG cells to drive clustered apical constriction (Chung et al., 2017; Fig. 1A). Yet, it is unknown how the Fog signal is sensed and transduced into downstream Rho1 signaling during epithelial tube formation.

Studies in early *Drosophila* embryos have suggested a role of GPCR signaling as a common module for Rho1 activation in different subcellular regions of the cell. In the mesoderm, Smog and Mist function together to activate myosin in the medioapical region of cells to drive apical constriction (Kerridge et al., 2016). In the ectoderm, where no apical constriction occurs, Smog is required for junctional myosin activation to drive cell intercalation (Kerridge et al., 2016). Recent work further has shown that distinct RhoGEFs activate myosin contractility in the apical and junctional domain of epithelial

101 cells under the control of specific G proteins in early *Drosophila* embryos (Garcia De
102 Las Bayonas et al., 2019). However, whether all three myosin pools in the SG are
103 regulated by independent mechanisms or by a common module during epithelial tube
104 formation remains unclear.

105 The contractile force of the actomyosin networks causes an increase of hydrostatic
106 pressure in the cytoplasm (Charras et al., 2005). During epithelial morphogenesis, cells
107 maintain the surface integrity by proper organization of actin at the cell cortex. Loss of
108 organized cortical actin networks leads to the formation of blebs, spherical protrusions
109 of the plasma membrane (Charras, 2008). During *Drosophila* gastrulation, blebs
110 occasionally arise during apical constriction of mesodermal cells; these blebs correlate
111 with apical F-actin holes (Costa et al., 1994; Jodoin et al., 2015). Disruption of cortical
112 actin by latrunculin B, which sequesters globular actin (G-actin) and prevents
113 filamentous actin (F-actin) assembly, enhances blebbing in epithelial cells in early
114 *Drosophila* embryos (Kanesaki et al., 2013). Mutations in heterotrimeric G proteins also
115 enhance blebbing (Kanesaki et al., 2013), suggesting a role of G proteins in stabilizing
116 cortical actin. The mechanisms of cortical actin regulation during epithelial tube
117 formation are not well understood.

118 Here, we reveal multiple roles of Smog GPCR in regulating actomyosin networks during
119 *Drosophila* SG tube formation. We show that the GPCR Smog transduces Fog signal to
120 regulate myosin contractility in the medioapical region of SG cells to drive apical
121 constriction during SG invagination. Our study supports a model wherein Smog
122 regulates medioapical and junctional/supracellular myosin pools in a Fog-dependent
123 and -independent manner, respectively. We further reveal new roles of Smog in
124 regulating the microtubule networks, key apical and junction proteins, and cortical actin
125 organization during SG invagination, suggesting multifunctional roles of GPCR signaling
126 during epithelial tube formation.

127 **RESULTS**

128 **Smog transduces Fog signal in the SG**

129 To test the role of Smog in transducing Fog signal during SG invagination, we first
130 examined *smog* transcripts and Smog protein levels in the developing SG. Consistent
131 with the ubiquitous expression of *smog* (Kerridge et al., 2016), fluorescent in situ
132 hybridization revealed low levels of *smog* mRNA expression in the entire embryo,
133 including the SG. Strong *smog* mRNA signals were observed in SG cells near the
134 invagination pit (Fig. 1B, B'), potentially due to the shrinking apical domain in those
135 cells. We also examined Smog protein localization in the SG using a functional Smog-
136 GFP fusion protein expressed under the control of the *sqh* promoter (Kerridge et al.,
137 2016). Smog-GFP signals were detected as small punctate structures enriched near
138 AJs in SG cells (Fig. 1C-C''; AJs were marked with the key AJ protein E-Cadherin (E-
139 Cad). Importantly, Smog-GFP signals were dramatically increased in the entire apical
140 domain of Fog-overexpressing SGs (Fig. 1D-D''; quantification in Fig. 1E), suggesting
141 that Smog is recruited to the apical domain of SG cells by overproduced Fog.

142 To test whether Smog transduces Fog signal in the SG to regulate myosin contractility,
143 we performed a genetic suppression test. We hypothesized that if Smog is a SG
144 receptor for Fog, knocking down *smog* in the SG should suppress the gain-of-function
145 effect of Fog. We used sqh-GFP, a GFP-tagged version of myosin regulatory light chain
146 (Royou et al., 2004), and Rok-GFP, a GFP-tagged Rok fusion protein (Abreu-Blanco et
147 al., 2014), as readouts of Fog signaling. sqh-GFP signals were significantly increased in
148 the medioapical region of Fog-overexpressing SG cells (compare Fig. 1G', G''' to Fig.
149 1F', F'''; quantification in Fig. 1H) but not at AJs (Fig. 1I), suggesting increased
150 medioapical myosin by Fog overexpression. Fog-overexpressing SG cells showed
151 highly distorted AJs (Fig. 1G'') compared to control SG cells (Fig 1F''), suggesting
152 increased pulling forces due to increased medioapical myosin in Fog-overexpressing
153 SG cells. Consistent with our finding that Fog signal promotes accumulation of Rok in
154 the medioapical region of SG cells (Chung et al., 2017), quantification of areas occupied
155 by Rok-GFP puncta revealed overaccumulated Rok-GFP signals in the medioapical
156 region of Fog-overexpressing SG cells (compare Fig. 1L', L''' to Fig. 1K', K'''';
157 quantification in Fig. 1N). Knockdown of *smog* in the SG using RNA interference (RNAi)

158 and the SG-specific *fkh-Gal4* driver (Henderson and Andrew, 2000) both suppressed
159 the medioapical accumulation of Rok-GFP signals and reduced the magnitude of AJ
160 distortion (Fig. 1M-M'''; quantification in 1N, O). These data suggest that Smog
161 transduces Fog signal in the SG to facilitate Rok and myosin accumulation in the
162 medioapical region of SG cells.

163

164 **Smog-transfected *Drosophila* S2 cells contract upon Fog signal**
165 To further test the role of Smog in transducing Fog signal to regulate myosin
166 contractility, we performed an in vitro cell contraction assay using *Drosophila* S2 cells.
167 S2 cells do not express Fog receptors, and therefore, do not respond to Fog in the
168 normal culture condition (Manning et al., 2013; Fig. 2A-B'). As shown in a previous
169 study (Manning et al., 2013), S2 cells transfected with Mist, the mesoderm-specific
170 receptor for Fog, contracted robustly when cultured in Fog-containing media (Fig. 2C-
171 D'). Since Smog was not detectable in *Drosophila* S2 cells (modENCODE Cell Line
172 Expression Data; Flybase), we tested if S2 cells transfected with Smog also contract
173 upon Fog treatment. Indeed, Smog-transfected cells showed a significantly higher
174 percentage of contraction upon Fog treatment compared to non-transfected S2 cells
175 (Fig. 2A-B', E-F'; quantification in Fig. 2G). Thus, Smog can transduce Fog signal to
176 regulate cellular contractility both in the SG and in vitro.

177

178 **Smog is required for apical constriction in the SG and epithelial morphogenesis**
179 **during embryogenesis**
180 To test the role of Smog in apical constriction of SG cells as a Fog receptor, we
181 knocked down *smog* in the SG (using *fkh-Gal4*) using RNAi and compared apical areas
182 of SG cells to those in *fog* mutants. Two independent short hairpin RNAi lines,
183 *TRiP.HMC03192* (a stronger line; Fig. 3B, B'; also used for genetic suppression assay
184 in Fig. 1M-M''') and *TRiP.GL01473* (a weaker line; Fig. S1G, G'), were used. *smog*
185 knockdown using either line reduced Smog-GFP signals in the SG, with a stronger
186 effect with *TRiP.HMC03192*, confirming the effect of the RNAi lines (Fig. S1A-D). Cell

187 segmentation analysis revealed that SG cells with smaller apical areas showed a less
188 coordinated spatial distribution in *smog* RNAi SGs compared to control (Fig. 3A-B'; Fig.
189 S1F-G'), similar to the previously reported *fog* mutant phenotype (Chung et al., 2017;
190 Fig. S1E, E'). However, quantification of percentage and cumulative percentage of cells
191 of different apical areas revealed different behaviors between *fog* and *smog*. In *fog*
192 mutants, the number of constricting cells is not significantly different from wild type
193 (WT), but cells with small apical areas are dispersed across the entire SG placode
194 (Chung et al., 2017). On the other hand, SGs with *smog* knockdown with either RNA
195 line showed larger apical areas compared to control (Fig. 3G; Fig. S1H). The difference
196 in apical constriction defects between *fog* mutants and *smog* knockdown suggests a
197 potential Fog-independent role of Smog.

198 Since *smog* has a strong maternal contribution (Flybase Developmental RNA-Seq), we
199 also knocked down *smog* both maternally (using *matα-Gal4*; Häcker and Perrimon,
200 1998) and zygotically in the SG (using *fkh-Gal4*) and observed slightly more severe
201 apical constriction defects in SG cells (hereafter referred to as *smog* M/Z knockdown;
202 Fig. 3C, C'; quantification in 3G). Maternal knockdown of *smog* using the stronger RNAi
203 line (*TRiP.HMC03192*) resulted in severe defects in egg-laying. Therefore, all M/Z
204 knockdown experiments were performed using the weaker line (*TRiP.GL01473*).
205 Consistent with the ubiquitous expression of *smog* and its role in epithelial
206 morphogenesis in the early *Drosophila* embryo (Kerridge et al., 2016), *smog* M/Z
207 knockdown resulted in a slight disruption of the overall embryonic morphology, including
208 defects in the head region, a wavy embryo surface, and an irregular ventral midline (Fig.
209 3M, N). Unlike the circular SG placode of WT, *smog* M/Z knockdown also resulted in a
210 SG placode elongated along the dorsal/ventral axis (compare Fig. 3A, A' to 3C, C'). 3D
211 reconstruction of confocal images revealed disrupted epithelial morphology in *smog* M/Z
212 knockdown, with wide and wavy grooves, enlarged epithelial cells, and an elongated SG
213 placode (Fig. 3I, J).

214 *smog* zygotic null mutants (Kerridge et al., 2016) had a range of defects similar to those
215 observed with *smog* knockdown. 73.8% of embryos (59/80) showed relatively normal
216 embryonic morphology with mild apical constriction defects in SG cells, like *smog*

217 zygotic knockdown (classified as '*smog* null [mild]'; Fig. 3D-E', K; quantification in 3H);
218 26.2% of embryos (21/80) showed a disrupted embryonic morphology with SGs
219 elongated along the dorsal/ventral axis (Fig. 3F, F', L) and more severe apical
220 constriction defects (Fig. 3H), like *smog* M/Z knockdown (classified as '*smog* null
221 [severe]'). All embryos at late stages (stages 15-17) *smog* null mutants showed
222 relatively normal embryonic morphology (Fig. S2A, B), suggesting that severely
223 defective embryos with *smog* loss do not survive/develop past stage 14. Notably, these
224 embryos have relatively normal internalized SGs (Fig. S2E-G), except for rare cases of
225 crooked SG morphology (Fig. S2C, D). Altogether, these data suggest that Smog is
226 required for coordinated apical constriction during SG invagination and proper epithelial
227 morphogenesis during embryogenesis.

228

229 **Smog regulates medioapical and junctional myosin in a Fog-dependent and -**
230 **independent manner in the SG**

231 We next examined myosin levels and distribution in the SGs in *smog* knockdown or
232 *smog* mutants using sqh-GFP. Medioapical myosin is the only myosin pool defective in
233 the SGs of *fog* mutants (Chung et al., 2017; Fig. S3A-E). Consistent with the idea that
234 Smog transduces Fog signal in the SG, *smog* knockdown (either zygotic or M/Z
235 knockdown) and *smog* loss resulted in a significant reduction in the intensity of
236 medioapical myosin in SG cells near the invagination pit, compared to control (Fig. 4A-
237 D''; quantification in 4I). Moreover, compared to clear web-like structures of medioapical
238 myosin in control SG cells (Fig. 4A-A''), SG cells in *smog* knockdown or *smog* null
239 mutants showed reduced areas of sqh-GFP puncta (Fig. 4L), with dispersed myosin
240 along the entire apical surface in *smog* M/Z knockdown SG cells (Fig. 4C-C'').
241 Interestingly, the intensity of junctional myosin was also significantly reduced in SG cells
242 with *smog* knockdown or *smog* loss, compared to control (Fig. 4A-D'', quantification in
243 4J). This phenotype is distinct from what was observed in *fog* mutants, where junctional
244 myosin was unaffected in SG cells (Chung et al., 2017; Fig. S3D). The ratio of
245 medioapical to junctional myosin intensity was significantly reduced in *smog* M/Z
246 knockdown but not in *smog* zygotic knockdown or *smog* null [mild] SGs (Fig. 4K). We

247 conclude that Smog is required for maintaining normal levels of both medioapical and
248 junctional myosin in the SG in a Fog-dependent and -independent manner, respectively.

249 We also tested Rok distribution in SG cells in *smog* RNAi and *smog* null mutants using
250 Rok-GFP. Whereas Rok-GFP formed large punctate structures in the medioapical
251 region in control SG cells (Fig. 4E-E''), Rok-GFP failed to accumulate and was
252 dispersed along the entire apical domain in SG cells in *smog* knockdown and *smog* null
253 mutants (Fig. 4F-H''; quantification in 4M), similar to the dispersed Rok-GFP distribution
254 observed in *fog* mutant SG cells (Chung et al., 2017). These data suggest that Smog is
255 required for Rok accumulation in the medioapical domain of SG cells.

256

257 ***smog* loss leads to defects in the tissue-level myosin cable**

258 Reduced myosin levels and the elongated SG placode in *smog* null [severe] embryos
259 led us to test the third pool of myosin in the SG, the supracellular myosin cable
260 surrounding the SG placode. Consistent with the idea that this myosin cable is under
261 tension (Chung et al., 2017; Röper, 2012), WT SGs showed a relatively smooth tissue
262 boundary (Fig. 4N-N''). *smog* null [mild] embryos also maintained a smooth SG
263 boundary comparable to WT (Fig. 4O-O''). However, SGs in *smog* null [severe] embryos
264 showed an irregular boundary and a less clear myosin cable (Fig. 4P-P'').

265 We calculated the circularity of the SG placode as a measure of smoothness and
266 tension of the SG boundary. The circularity of the WT placode was significantly higher
267 than the circularity of one cell row inside (inner boundary) or outside of the SG placode
268 (outer boundary), suggesting a higher tension of the myosin cable in WT (Fig. 4Q, R).
269 The circularity of the placode of *smog* null [mild] embryos was comparable to WT (Fig.
270 4R). However, the circularity of the SG placode in *smog* null [severe] embryos was
271 significantly lower than that of WT and was not statistically significant from the inner or
272 outer boundaries, suggesting a lack of tension at SG boundary in *smog* null [severe]
273 mutants (Fig. 4R). Consistent with our previous study (Chung et al., 2017), *fog* mutants
274 did not show defects in the myosin cable (Fig. S3F-H), even in the severely twisted
275 embryos with extra grooves and folds. Overall, our data suggest that, unlike *fog*, the

276 loss of *smog* affects all myosin pools in the SG, including the myosin at the SG
277 boundary, leading to reduced tension at the SG boundary and defects in generating the
278 compressing force.

279

280 **Smog is required for proper localization of apical and junctional components and**
281 **microtubule networks in epithelial cells**

282 Since we observed a range of defects in whole embryo morphology in *smog* mutants,
283 we explored the potential cellular basis. In stage 11 *smog* null [severe] embryos, we
284 occasionally observed large areas in the epidermis where E-Cad (Fig. 5B, B'; compare
285 to WT in Fig. 5A, A') and the apical determinant protein Crumbs (Crb) (Fig. 5D, D';
286 compare to WT in Fig. 5C, C') signals were absent or significantly reduced. Relatively
287 strong signals of the cell membrane marker Gap43-mCherry (Martin et al., 2010) were
288 observed in these regions (Fig. 5E-E''), suggesting that the cell membrane is still intact.
289 Cells in these regions had enlarged apical areas compared to neighboring cells with
290 strong E-Cad signals (Fig. 5E-E''), suggesting reduced epithelial tension and/or integrity
291 in cells with reduced E-Cad levels. Similarly, in late-stage (stage 14) embryos, Crb
292 levels were significantly reduced in large areas; in the most severe cases, Crb was
293 dispersed in the entire epidermis (Fig. S4B, B'). These data suggest that Smog is
294 required for maintaining epithelial polarity and junctional integrity by regulating E-Cad
295 and Crb levels or distribution.

296 To better understand the basis of the reduced E-Cad and Crb in *smog* mutants, we
297 examined *smog* null mutant SG cells at higher magnification. Even in SGs that do not
298 contain large patches of E-Cad/Crb loss, E-Cad/Crb signals were discontinuous, with
299 small gaps in signal along the cell boundary (Fig. 5F-O). Such gaps were observed in
300 both *smog* null [mild] and *smog* null [severe] embryos. Although the number and the
301 length of gaps in E-Cad signals in *smog* null [mild] were comparable to those of WT,
302 they were significantly higher in *smog* null [severe] compared to WT (Fig. 5G, H;
303 quantification in 5L, M). The number and the length of gaps in Crb signals in SG cells
304 were significantly higher in both mild and severe *smog* null mutant embryos compared

305 to WT (Fig. 5J, K; quantification in 5N, O). These data suggest a role of Smog in
306 regulating Crb and E-Cad levels and continuity during epithelial morphogenesis,
307 including the SG.

308 Anisotropic localization of Crb at the SG boundary has been suggested to drive the
309 formation of supracellular myosin cable in SG (Röper, 2012). Consistent with this, in
310 control SGs, Crb levels were higher in inside junctions that do not contribute to the
311 myosin cable, whereas myosin was highly enriched at the junction forming the cable at
312 the SG boundary (Fig. S4C-E'''). However, in *smog* null [severe] SGs, the overall Crb
313 intensity was quite low, and Crb did not show an anisotropic localization at the SG
314 boundary (Fig. S4F-H'''). This data suggests that *smog* loss results in the reduction of
315 both myosin and Crb, failing to form the supracellular myosin cable at the SG boundary.

316 Microtubules are required for forming and maintaining apical myosin structures (Booth
317 et al., 2014; Ko et al., 2019) and for transporting several key apical and junctional
318 proteins in *Drosophila* tubular organs, including E-Cad and Crb (Le and Chung, 2021; le
319 Droguen et al., 2015). We recently showed that microtubule-dependent intracellular
320 trafficking has an important role in regulating apical constriction and medioapical myosin
321 during SG invagination (Le and Chung, 2021). To examine the microtubule networks in
322 the SG of WT and *smog* mutant embryos, we stained with antibodies against acetylated
323 α-tubulin (Ace-tub), a marker of stable, long-lived microtubules, and tyrosinated α-
324 tubulin (Tyr-tub), a marker of dynamic, short-lived microtubules (Westermann and
325 Weber, 2003). Compared to WT, both Ace-tub and Tyr-tub signals were reduced in
326 *smog* mutants (compare Fig. 5Q, R, U, V to Fig. 5P, T), with a dramatic reduction in
327 Ace-tub levels in *smog* null [severe] embryos (Fig. 5R), suggesting disrupted
328 microtubule networks in *smog* mutants. The reduced Ace-tub and Tyr-tub signals were
329 more prominent in the SG compared to the surrounding epithelial cells; the ratio of Ace-
330 tub and Tyr-tub intensity in SG cells to the intensity in cells outside the SG was
331 significantly decreased in *smog* mutants compared to WT (Fig. 5X, Y). A slight but less
332 prominent reduction in Ace-tub and Tyr-tub signals was also observed in the SG in *fog*
333 mutants (Fig. 5S, W; quantification in 5X, Y). Overall, this finding suggests that loss of

334 *smog* could affect apical pools of myosin, Crb and E-Cad through effects on microtubule
335 abundance, distribution and/or polarity.

336

337 **Smog is required for cortical actin organization in the SG**

338 We observed numerous blebs in the apical membrane of SG cells in *smog* null [severe]
339 mutants, which were most prominent near the invagination pit (compare Fig. 6A-A''' to
340 Fig. 6B-B'''). Such blebs were not observed in SGs in WT, *smog* null [mild], or *fog*
341 mutant embryos (Fig. S5A-C''). Rok-GFP was enriched in many of these blebs (Fig. 6B-
342 B'''), consistent with Rok's recruitment to retracting blebs (Aoki et al., 2016). In *smog*
343 null [severe] embryos, blebs were also occasionally observed in cells outside the SG
344 placode (Fig. S5D-E''). During *Drosophila* gastrulation, bleb formation correlates with
345 cortical F-actin holes (Jodoin et al., 2015), and disruption of cortical actin enhances
346 blebbing (Kanesaki et al., 2013). We therefore tested if Smog affects the cortical actin
347 network during apical constriction in the SG. Indeed, phalloidin staining revealed that
348 whereas strong F-actin signals were observed in the apical domain of SG cells near the
349 invagination pit in WT, F-actin was reduced in SGs in *smog* mutants (Fig. 6C-E).

350 Apical F-actin formation in *Drosophila* tubular organs requires the formin family actin
351 nucleator Diaphanous (Dia) (Massarwa et al., 2009; Rousso et al., 2013). Since the
352 apical localization and activity of Dia are critical for restricting F-actin formation to the
353 correct membrane domain, we tested the localization and levels of Dia in the SG in
354 *smog* mutants. Similar to reduced F-actin (Fig. 6C-E), we observed reduced Dia signals
355 in the apical domain of SG cells in *smog* mutants, compared to WT (Fig. 6G-I).
356 Quantification of Dia levels revealed that the overall Dia intensity is reduced in the SG
357 placode in *smog* mutants, with a stronger effect in the *smog* null [severe] than *smog* null
358 [mild] embryos (Fig. 6K). SGs in *fog* mutants appeared to show a slight reduction of F-
359 actin (Fig. 6F), but Dia levels in *fog* mutants were comparable to WT (Fig. 6J, K). Our
360 data suggest that Smog is required for the cortical actin networks during SG
361 invagination, at least in part via modulating Dia levels.

362 We next tested if the reduction in actin levels in *smog* mutants is due to defects in actin
363 turnover. To test this, we modulated the level of actin regulators in the SG in *smog*
364 mutants and assayed the blebbing phenotype. Using RNAi, we knocked down
365 *chickadee* (*chic*), which encodes *Drosophila* profilin, a protein that increases F-actin by
366 promoting actin polymerization (Cooley et al., 1992), in the *smog* mutant background. If
367 there is a shift from F-actin to monomeric G-actin in *smog* mutants, we expect
368 enhancement of the disorganized actin phenotype and bleb formation with a reduced
369 *chic* level. Blebs were not observed in *smog* null [mild] embryos or in SGs knocked
370 down for *chic* in the otherwise wild-type background (Fig. 6L-M''). However, when *chic*
371 was knocked down in the SG in the *smog* mutant background, we observed enhanced
372 blebbing even in SG cells in *smog* null [mild] embryos (Fig. 6N-N''). Since profilin
373 promotes formin-mediated actin filament assembly (Romero et al., 2004; Zweifel and
374 Courtemanche, 2020), our data suggests that reduced profilin by *chic* knockdown
375 aggravated defects in cortical actin organization with reduced Dia in *smog* mutants.
376 Overall, our data suggest that Smog is required for cortical actin organization as well as
377 myosin activation during epithelial morphogenesis.

DISCUSSION

Smog regulates different pools of myosin in a Fog-dependent and -independent manner during SG invagination

Fog signaling triggers epithelial cell shape changes driving tissue folding and invagination during development of *Drosophila* and other insects (Benton et al., 2019; Manning and Rogers, 2014). During *Drosophila* embryogenesis, *fog* is upregulated in multiple tissues undergoing apical constriction and tissue invagination, such as ventral furrow (mesoderm), the posterior midgut (endoderm), and the SG (ectodermal derivative) (Nikolaidou and Barrett, 2004). During *Drosophila* gastrulation, the ubiquitously expressed GPCR Smog and the mesoderm-specific GPCR Mist respond to Fog signal to regulate myosin contractility during mesoderm invagination (Kerridge et al., 2016; Manning et al., 2013). Here, we provide evidence that Smog functions as a SG receptor for Fog to activate myosin during SG invagination. Knockdown of *smog* by RNAi suppresses the gain-of-function effect of Fog in the SG (Fig. 1). Also, Smog-transfected S2 cells contract upon Fog signal (Fig. 2), suggesting that Smog responds to Fog to regulate myosin contractility both in vivo and in vitro. Our data show that Fog overexpression leads to Smog recruitment to the medioapical region of SG cells (Fig. 1). Consistent with our data, Fog overexpression induces oligomerization of Smog in early *Drosophila* embryos (Jha et al., 2018).

Our study also dissects the roles of Smog in myosin activation during SG morphogenesis and reveals Fog-independent roles of Smog. Whereas *fog* mutants exhibit a decrease in only the medioapical myosin pool in SG cells (Chung et al., 2017; Fig. S3), *smog* loss and SG-specific knockdown of *smog* result in a significant reduction of both medioapical and junctional myosin (Fig. 4). We propose that Smog regulates junctional myosin during epithelial morphogenesis in response to an unknown, ubiquitously expressed ligand and regulates medioapical myosin in response to Fog in tissues with high Fog signals, such as the mesoderm (Kerridge et al., 2016; Manning et al., 2013) and the SG (this study). Consistent with this model, during *Drosophila* gastrulation, Smog activates different myosin pools in tissues with different Fog levels. In the mesoderm, where Fog levels are high, Smog and Mist transduce Fog signal to activate myosin in the medioapical region and drive apical constriction. In the ectoderm,

409 where Fog levels are very low, Smog is required for junctional myosin activation to drive
410 cell intercalation. SG cells undergo both apical constriction and cell intercalation, and
411 our data shows that Smog regulates both pools of myosin in the SG in a Fog-dependent
412 and -independent manner. It is possible that in tissues with high Fog signals, an
413 additional tissue-specific GPCR(s) function with Smog in response to Fog to fine-tune
414 the Fog signaling for proper apical constriction, like Mist does in the mesoderm. It will be
415 interesting to determine whether additional SG-specific GPCRs function with Smog
416 during SG invagination.

417 The downstream components that transduce signals from the Smog GPCR to regulate
418 myosin in distinct regions of SG cells await discovery. Good candidates include two Rho
419 guanine nucleotide exchange factors (RhoGEFs), RhoGEF2 and Dp114RhoGEF, which
420 have been shown to activate Rho1 signaling at the medioapical and junctional domain
421 of epithelial cells, respectively (Garcia De Las Bayonas et al., 2019). This process
422 requires upstream activation by heterotrimeric G proteins $G\alpha_{12/13}$/Cta and Gβ13F/Gγ1 at
423 the medioapical and junctional domains, respectively (Garcia De Las Bayonas et al.,
424 2019). Thus, distinct ligand-receptor binding with Smog may activate distinct G proteins
425 and/or RhoGEFs in the medioapical and junctional domains.

426

427 **Smog regulates cortical actin organization during SG invagination**
428 We also discover that Smog regulates cortical F-actin organization during SG
429 invagination (Fig. 6). *smog* loss significantly reduces levels of F-actin and the formin
430 protein Dia (Fig. 6). Rho1 regulates actin polymerization via Dia (Goode and Eck, 2007),
431 and apical F-actin formation in the *Drosophila* SG requires apical localization and
432 activity of Dia (Massarwa et al., 2009; Rousso et al., 2013). Our data suggest that Smog
433 activates Rho1 signaling to regulate both cortical F-actin (via Dia) and myosin (via Rok)
434 (Fig. 7). *fog* mutants also show slightly reduced F-actin and Dia levels, to a similar level
435 to *smog* null [mild] embryos (Fig. 7), and these embryos do not show membrane
436 blebbing (Fig. 7; Fig. S5). It is possible that Smog regulates cortical actin in both Fog-
437 dependent and independent manners and perhaps subtle changes in Dia and F-actin

438 levels in *fog* mutants are not enough to cause membrane blebbing. Alternatively,
439 Smog's role in regulating cortical actin is independent of Fog; reduced F-actin levels in
440 *fog* mutants may be a secondary effect due to a defective medioapical myosin pool.
441 During *Drosophila* gastrulation, *fog* mutants show normal GFP-Moesin signals in the
442 ventral furrow, suggesting normal cortical actin organization upon *fog* loss (Kanesaki et
443 al., 2013). $G\alpha_{12/13}$/Cta is a key component downstream of Fog that recruits RhoGEF2 to
444 the apical membrane to regulate myosin contractility (Barrett et al., 1997; Dawes-Hoang
445 et al., 2005). Interestingly, mutations in Gαi (G-iα65A) and Gβ13F/Gγ1, but not
446 $G\alpha_{12/13}$/Cta, disrupt cortical actin organization in early *Drosophila* embryos (Fox and
447 Peifer, 2007; Kanesaki et al., 2013). Therefore, Smog may signal through Gαi and/or
448 Gβ13F/Gγ1 to organize cortical actin, independent of Fog and $G\alpha_{12/13}$/Cta.

449 The link between heteromeric G proteins and Rho1 signaling occurs through activation
450 of specific RhoGEFs (Vázquez-Victorio et al., 2016). Actin polymerization resulting from
451 Fog-independent Smog activation may imply the recruitment of distinct proteins
452 modulating the activation of Rho1-mediated pathways. For example, in the absence of
453 Fog, a specific RhoGEF(s) downstream of Gαi or Gβ13F/Gγ1 may link Smog and Rho1
454 signaling to regulate cortical actin organization; upon high Fog signals, a different Rho1
455 modulator(s) downstream of $G\alpha_{12/13}$/Cta may be recruited to facilitate medioapical
456 myosin formation. Further work is needed to identify the link between Smog and Rho1
457 activation in the presence or absence of Fog during SG invagination. It will be also
458 interesting to determine whether Fog-independent roles of Smog–regulating cortical
459 actin and junctional myosin–involve common or distinct Rho1 modulators.

460

461 **Smog regulates epithelial integrity during development**

462 *smog* null mutant embryos show a range of defects, allowing us to dissect the roles of
463 Smog in epithelial morphogenesis. Our data reveal that Smog is required for epithelial
464 integrity by affecting levels and localization of Crb and E-Cad (Fig. 5). Since the
465 decrease in the level of Crb and E-Cad in *smog* mutants correlates with significantly
466 reduced myosin levels, disrupted epithelial integrity may be due to disrupted actomyosin

467 networks. Myosin II is critical for cells to concentrate E-cad at cell-cell contacts (Shewan
468 et al., 2005). In early *Drosophila* embryos, the absence of contractile myosin leads to
469 the disassembly of junctions (Weng and Wieschaus, 2016). A possible scenario is that
470 Smog is required to recruit key Rho1 regulators, such as RhoGEF2, Dp114RhoGEF, or
471 other SG-upregulated RhoGEFs, to AJs during SG invagination to promote junctional
472 myosin assembly. Since Dia helps coordinate adhesion and contractility of actomyosin
473 (Homem and Peifer, 2008) and formin-mediated actin polymerization at AJs stabilizes
474 E-Cad and maintains epithelial integrity (Rao and Zaidel-Bar, 2016), reduced Dia levels in
475 *smog* mutants may also contribute to loss of epithelial integrity.

476 Reduced and discontinuous signals of apical and junctional components in *smog*
477 mutant embryos can also be due, in part, to compromised intracellular trafficking.
478 Disorganized microtubule networks in SGs in *smog* mutants (Fig. 5) support this idea.
479 Our recent study showed that microtubule- and Rab11-dependent intracellular
480 trafficking regulates apical myosin pools and apical constriction during SG invagination,
481 via apical enrichment of Fog and the continuous distribution of Crb and E-Cad along
482 junctions (Le and Chung, 2021). The mechanism of how Smog affects microtubule
483 organization remains to be revealed. *fog* mutants also show slightly disrupted
484 microtubule networks, albeit less prominently than *smog* null [severe] (Fig. 5). Whether
485 this is a direct effect of loss of *fog* or an indirect result of the disrupted medioapical pool
486 of myosin remains to be answered. Overall, our findings suggest the multifaceted roles
487 of Smog during epithelial tube formation in regulating distinct myosin pools and cortical
488 actin in different subcellular domains in a ligand-dependent manner.

489 **MATERIALS AND METHODS**

490 **Fly stocks and genetics**

491 The fly stocks used in this study are listed in Table S1. All the crosses were performed
492 at 25°C.

493

494 **Immunofluorescence and confocal microscopy**

495 *Drosophila* embryos were collected on grape juice agar plates supplemented with yeast
496 paste at 25℃. Embryos were dechorionated with 50% bleach. For most samples,
497 embryos were fixed in 1:1 heptane: formaldehyde for 40 minutes and devitellinized with
498 80% ethanol. For Rok-GFP, sqh-GFP, and phalloidin staining, embryos were hand-
499 devitellinized. Embryos were then stained with primary and secondary antibodies in
500 PBSTB (1X PBS with 0.1% Triton X-100 and 0.2% bovine serum albumin) and PBTr
501 (1X PBS with 0.1% Triton X-100) for ethanol devitalization and hand-devitalization,
502 respectively. Antibodies used in our experiments are listed in Table S2. Embryos were
503 mounted in Aqua-Poly/Mount (Polysciences, Inc) and imaged with a Leica TCS SP8
504 confocal microscope using 63x, NA 1.4 and 40x, NA 1.3 objectives. Images were
505 acquired as z-stacks (each 0.3 μm apart) that span the apical and junctional domains of
506 cells in the SG placode.

507

508 **Fluorescent in situ hybridization**

509 Embryos were fixed using formaldehyde/heptane for 30 min followed by devitellinization
510 with methanol. SP6 polymerase-synthesized digoxigenin (DIG)-labeled antisense probe
511 was prepared using the following primers: *smog*-F, 5'-ACAGAGCCCACCTGTGTAGG-
512 3'; *smog*-R, 5'-TCGCTGATCGAAAATGATCTC-3'. Fluorescent in situ hybridization was
513 performed using standard methods as described in (Knirr et al., 1999). Briefly, the
514 embryos were pre-hybridized for 1 hour at 56°C post-fixation. Following this step, the
515 embryos were hybridized with the probe overnight at 56°C. The next day, embryos were
516 stained for DIG using the anti-DIG primary antibody and biotin-conjugated secondary
517 antibody. The embryos were then incubated with AB solution (PK-6100, VECTASTAIN
518 Elite ABC kit). Tyramide signal amplification reaction was performed using Cy3
519 fluorescent dye (diluted 1:50 using amplification diluent) (Perkin Elmer Life Sciences,

520 Inc., NEL753001kt). The embryos were co-stained with CrebA and Crb antibodies for
521 visualizing SG nuclei and apical cell boundaries, respectively.
522
523 **Total Smog-GFP and Dia intensity**
524 For Smog-GFP quantification, maximum intensity projections of two z-sections that
525 span the apical and the junctional region of SG cells were used. Intensity means of
526 Smog-GFP signals of SG cells in the entire SG placode were measured using Imaris
527 software (Bitplane). The mean intensity of Smog-GFP was normalized by the median
528 deviation. The integrated density of Smog-GFP was calculated by multiplying the apical
529 area of the cell with the mean intensity of each cell. Total Smog-GFP signals within the
530 whole placode were calculated as the sum of the integrated density of all cells. For
531 background correction, mean gray values of Smog-GFP in ten cells outside of the SG
532 placode were measured using ImageJ (NIH). The average value of mean gray values of
533 Smog-GFP in these ten cells was used to subtract the background of the cells inside the
534 placode from the same embryo. Five SGs were used for quantification for each
535 genotype except for control in Fig. 1E, where four SGs were used. Statistical
536 significance was determined using Mann-Whitney U test in the GraphPad Prism
537 software.

538 For total Dia intensity quantification, maximum intensity projection of two z-sections of
539 the most apical region of SG cells was used. The images were then exported to ImageJ
540 and converted to the RGB stack image type. Mean gray values of Dia signals in the
541 whole placode were measured. For background subtraction, the average mean gray
542 value of Dia signals for ten cells outside the SG placode was subtracted from the mean
543 gray value of Dia intensity of the whole SG placode. These values were scaled by the
544 mean normalization. The total Dia intensity in the whole placode was calculated by
545 multiplying the normalized intensity with the entire area of the placode. Statistical
546 significance was determined using Mann-Whitney U test.

547
548 **Cell segmentation and apical area quantification**

549 SGs that were invaginated within the range of 4.8-9.9 μm depth were used for
550 quantification. Two or three z-sections of the apical domain were used to generate a
551 maximum intensity projection (Leica LasX software). SG cells were marked using CrebA
552 and segmented along E-Cad signals using the Imaris program. Apical areas of
553 segmented cells were calculated using Imaris, and cells were color-coded based on
554 their apical domain size. Frequency distribution was performed using GraphPad Prism.
555 Apical areas from eight SGs were quantified in control, *smog* knockdown (Z), and *smog*
556 null [mild] embryos. Six SGs were used for quantification for *smog* knockdown (M/Z)
557 and *smog* null [severe] embryos. Statistical significance was determined using Mann-
558 Whitney U test (percentage of cells) and Kolmogorov-Smirnov test (cumulative
559 percentage of cells).
560
561 **Quantification of myosin intensity in the medioapical and junctional domains**
562 Maximum intensity projection of two z-sections spanning apical and junctional regions of
563 SG cells with sqh-GFP and E-Cad signals was used. The images were then exported to
564 ImageJ and converted to RGB stack image type. Twenty cells near the invagination pit
565 in each of five SGs were used for quantification. To calculate the medioapical and
566 junctional myosin intensity, regions were drawn manually along the inner and outer
567 boundary of the E-Cad signal of each cell, and mean gray values were measured for
568 medioapical and junctional myosin. For background subtraction, the average mean gray
569 value of sqh-GFP signals for ten cells outside the SG placode was subtracted from the
570 mean gray value of medioapical and junctional myosin for each SG cell. SuperPlots
571 (Lord et al., 2020) were used to address the variability of datasets in each SG. Each
572 data point in the graph represents one SG consisting of twenty cells used for
573 quantification. Statistical significance was determined using Welch's t-test. A normal
574 distribution was tested using Jarque-Bera test (Microsoft Excel) or a bell-shape of data
575 distribution by making a histogram.
576
577 **Quantification of areas of Rok-GFP and medioapical myosin particles**
578 A single z-section of the confocal image with the strongest Rok-GFP signals in the
579 medioapical region was used. Rok-GFP signals were converted to black and white

using the threshold tool in Adobe Photoshop. Junctional Rok-GFP signals were removed manually based on E-Cad signals. Areas of Rok-GFP puncta were determined using the Analyze Particles tool in ImageJ. Rok-GFP puncta with area ≥0.02 μm^2 was measured. Fifteen cells in the dorsal posterior region near the invagination pit of the SG placode were used for quantification. The same strategy was used for sqh-GFP signals to quantify the area of medioapical myosin. SuperPlots show mean values of data points of five SGs. Statistical significance was determined using Mann-Whitney U test.

Quantification of the waviness of junctions

Using a single z-section with the highest E-Cad signals and ImageJ software, the shortest (L_0) and the actual distance (L) between vertices were measured in SG cells. The ratio of these distances (L/L_0) was used as the waviness of junctions. 10-15 cells near the invagination pit in each of five SGs were used for quantification. Statistical significance was determined using Mann-Whitney U test.

Circularity of the SG boundary

Using confocal images and ImageJ, cell boundaries were manually drawn along E-Cad signals at the SG placode boundary and one cell row outside and inside the placode. For most samples, strong myosin cable signals at the dorsal, anterior, and posterior boundaries of the placode and CrebA signals in SG cells were used to determine the SG boundary. In *smog* null [severe], where myosin signals were significantly reduced in all cells, CrebA signals were used to determine the boundary. The ventral midline was used as the ventral boundary of the SG in all cases. The perimeter and the area of the SG corresponding to these boundaries were measured using ImageJ, and circularity was calculated using the formula, $C = 4\pi \text{ area}/\text{perimeter}^2$. For a perfect circle, the value of circularity should be 1. Five SGs were used for quantification, and statistical significance was determined using Welch's t-test.

Quantification of number and length of gaps of Crb and E-Cad

The number and the length of gaps for Crb and E-Cad signals were measured using confocal images and ImageJ. A single z-section with the highest Crb or E-Cad signals

611 was chosen for quantification. Gaps with a length ≥0.2 μm were used for quantification.
612 All junctions from ten cells in five SGs were quantified. If there were multiple gaps on a
613 junction, we added the length of all the gaps on that junction to calculate the ratio of the
614 length of gaps to junctional length. Statistical significance was determined using Mann-
615 Whitney U test.
616
617 **Acetylated and tyrosinated α-tubulin intensity quantification**
618 Three z-sections spanning the most apical region of SG cells were used for
619 quantification. The SG boundary was drawn manually based on the E-Cad and CrebA
620 signals. The mean gray value of Ace-tub signals in the whole SG placode and ten cells
621 outside the SG of the same embryo was measured using ImageJ. The ratio of the mean
622 gray value of Tyr-tub signals inside the placode to the average mean gray value of cells
623 outside the placode was calculated and plotted. The same method was used for Tyr-
624 tub. Five SGs for each genotype were used for quantification. Mann-Whitney U test was
625 used to calculate the p values.
626
627 **Cell contractility assay**
628 cDNA clones for *smog* (RE70685) and *mist* (RE13854) were obtained from *Drosophila*
629 Genomics Resource Center (DGRC). Isolated cDNAs were cloned in-frame with the V5
630 tag into the pMT-V5-HisB vector (Addgene) using the conventional restriction digestion
631 and ligation method. Primers with restriction sites used to isolate the open reading
632 frame are stated below (restriction sites underlined).

633 *smog* CDS-EcoRI-5', 5'-CCGGAATTCATGGAACTGTGCATAGCAAC-3'
634 *smog* CDS-NotI-3', 5'-ATTTGCGGCCGCATTGGTCGTGATTGTATCTTTGG-3'
635 *mist* CDS-EcoRI-5', 5'-CCGGAATTCATGGACAGGAGTCGGAGTAGC-3'
636 *mist* CDS-NotI-3', 5'-ATTTGCGGCCGCAGCAAATGGTCTCCATTTTG-3'

637 S2 and S2-Mt-Fog-myc cells (Manning et al., 2013) were obtained from DGRC. Cells
638 were tested for contamination regularly. Shields and Sang M3 insect media (HiMedia)
639 was used with 10% Fetal Bovine Serum (Corning) and 1:1000 Antibiotic-Antimycotic
640 (Gibco). Cells were cultivated at 25°C either in 25-cm^2 flask in 5 ml media or 75-cm^2

641 flask in 15 ml media. To prepare for the Fog media, S2-Mt-Fog-myc cells were grown
642 undisturbed for 4-8 days to attain approximately 100% confluency. 50 µl of 100 mM
643 CuSO4 was added to nearly 100% confluent cells in 75-cm^2 flask to induce
644 metallothionein promoter. The Fog-containing media was collected by centrifugation
645 and further concentrated using 3,000 MW concentrators. The presence of Fog was
646 confirmed by Western blot using the Myc-antibody (Invitrogen; RRID:AB_2533008).
647 Non-transfected S2 cells were used as a control.

648 Cell contractility assay was performed as described in (Manning et al., 2013). Smog- or
649 Mist-transfected S2 cells were induced with $CuSO_4$. Cells were then transferred to
650 Concanavalin A-coated coverslips and fixed using 10% paraformaldehyde in PBTr for
651 15 minutes at room temperature. After being blocked in 5% NGS in PBTr for 20 minutes
652 at RT, cells were stained with the V5 antibody (Invitrogen; RRID:AB_2556564) to
653 differentiate between transfected and non-transfected cells. Cell contractility of
654 transfected cells was monitored using a phase-contrast filter in a Leica DM2500
655 microscope using the 40X, 0.8 NA objective. Three independent experiments were
656 performed. Two-way ANOVA was performed to calculate statistical significance.
657

Acknowledgments

We thank the members of the Chung laboratory for their comments and suggestions. We thank A. Martin, T. Lecuit and the Bloomington stock center for fly stocks, and D. J. Andrew and the Developmental Studies Hybridoma Bank for antibodies. We thank Flybase for the gene information. We are grateful to D. J. Andrew, C. D. Hanlon, J. Kim, and J. Matthew for their helpful comments on the manuscript. This work is supported by a start-up fund from Louisiana State University and grants from the Louisiana Board of Regents Research Competitiveness Subprogram and the National Science Foundation (MCB 2141387) to S.C.

667 **Figure Legends**

668 **Figure 1. Smog transduces Fog signal to activate Rok and myosin in the SG.** (A)
669 Cartoon diagram showing SG placodes (magenta) in the ventral side of a stage 11
670 *Drosophila* embryo. Cells that undergo apical constriction near the invagination pit
671 (asterisk) are shown in purple. In those cells, the Fog ligand (yellow) binds to its GPCR
672 (blue) to activate medioapical myosin. In all stage 11 SG images, anterior is to the left,
673 and dorsal is up. (B, B') Fluorescent in situ hybridization of *smog* (magenta) in the WT
674 SG. Arrowsheads, strong *smog* mRNA signals in apically constricting SG cells. Arrows,
675 *smog* signals near the grooves and the ventral midline. Green, CrebA (SG nuclei).
676 White lines, SG boundary. (C-D'') Smog-GFP (green) signals in control (C-C'') and Fog-
677 overexpressing SGs (D-D''). Magenta, E-Cad. Yellow arrowheads, puncta of Smog-GFP
678 signals in the apical region near AJs in control SG cells. Rred arrowheads, considerably
679 higher Smog-GFP signals in the entire apical domain of Fog-overexpressing SG cells.
680 Insets, magnified images of yellow boxed regions. (C'', D'') z-sections across the yellow
681 lines in C and D. (E) Quantification of total Smog-GFP intensity. n=4 SGs (control); 5
682 SGs (Fog overexpression). *p≤0.05 (Welch's t-test). (F-G''') sqh-GFP (green) and E-
683 Cad (magenta) signals in control (F-F''') and Fog-overexpressing (G-G''') SGs. (F'-G''')
684 Magnified images of yellow boxed regions in F and G. Yellow arrowheads, AJs. Cyan
685 arrowheads, sqh-GFP signals. (H-J) Quantification of medioapical myosin intensity (H),
686 junctional myosin intensity (I), and the ratio of medioapical to junctional myosin intensity
687 (J). ns, non-significant; *p≤0.05; **p≤0.01 (Welch's t-test). (K-M''') Rok-GFP (green) and
688 E-Cad (magenta) signals in SGs. K'-M''', magnified images of yellow boxed regions in
689 K-M. Yellow arrowheads, AJs. Cyan arrowheads, Rok-GFP puncta. (N, O)
690 Quantification of the area of Rok-GFP particles (N) and waviness of AJs (O). Asterisks,
691 invagination pit. n=5 SGs, 75 cells for each genotype in H-J, N, and O. **p≤0.01 (Mann-
692 Whitney U test).

693

694 **Figure 2. Smog-transfected S2 cells contract in response to Fog**. (A-F') S2 cells
695 cultured in the absence (A, C, E) or presence (B, D, F) of Fog. (A-B') Non-transfected.
696 (C-D') Mist-transfected. (E-F') Smog-transfected. A-F, phase contrast; A'-F', merged
697 images of phase contrast and V5 signals for transfected cells (green). White arrowhead

698 in E', a Smog-transfected S2 cell not contracting in the absence of Fog. Magenta
699 arrowheads, contracting cells. (G) Quantification of percentage of contracting cells
700 among the transfected cells. n=~100 cells per condition from three independent
701 experiments. ****p≤0.0001 (Two-way ANOVA with Tukey's multiple comparison post
702 hoc analysis).
703
704 **Figure 3. *smog* knockdown and loss result in apical constriction defects in the SG**
705 **and disrupted epithelial morphology.** (A-F') Confocal images of stage 11 SGs
706 stained for E-Cad (A-F) and corresponding heat maps of apical areas (A'-F').
707 *TRiP.HMC03192* and *TRiP.GL01473* are used for zygotic and M/Z knockdown of *smog*,
708 respectively. Red and white lines, SG boundary. (G, H) Quantification of percentage
709 (left) and cumulative percentage (right) of cells with different apical areas. Mann-
710 Whitney U test (for percentage of cells) and Kolmogorov-Smirnov test (for cumulative
711 percentage of cells). n=8 SGs (control, 902 cells; *smog* RNAi (Z), 823 cells; *smog* RNAi
712 (M/Z), 881 cells; WT, 892 cells; *smog* null [mild], 859 cells); 6 SGs (*smog* null [severe],
713 672 cells). ***p<0.001; ****p<0.0001. (I-L) 3D reconstruction of confocal z-sections of
714 SGs (Imaris) for WT (I), M/Z knockdown of *smog* (J), *smog* null [mild] (K), and *smog* null
715 [severe] (L). Green, E-Cad. Magenta, CrebA. Asterisks, invagination pit. Arrows in J and
716 L, exaggerated grooves. Arrowheads in J and L, enlarged SG cells. (M, N) Tile scan
717 confocal images of stage 11 embryos in WT (M) and M/Z knockdown of *smog* (N).
718 Green, E-Cad. Magenta, CrebA. Arrows, the ventral midline. Arrowheads, SGs.
719
720 **Figure 4. *smog* regulates all three pools of myosin in the SG in a Fog-dependent**
721 **and -independent manner.** (A-D'') Confocal images of stage 11 SGs with sqh-GFP
722 (green) and E-Cad (magenta) signals. (A'-D'') Higher magnification of the yellow boxed
723 region in A-D. (E-H'') Confocal images of SGs with Rok-GFP (green) and E-Cad
724 (magenta) signals. (E'-H") Magnified images of the yellow boxed region in E-H. (I-M)
725 Quantification of medioapical myosin intensity (I), junctional myosin intensity (J), ratio of
726 medial and junctional myosin intensity (K), area of medioapical myosin particles (L), and
727 area of Rok-GFP particles (M). ns, non-significant; *p≤0.05; **p≤0.01 (Welch's t-test for
728 I-K; Mann-Whitney U test for L and M). n=5 SGs, 100 cells (I-L) and 5 SGs, 75 cells (M)

729 for each genotype. (N-P'') Confocal images of SGs with sqh-GFP (green) and E-Cad
730 (magenta) signals. Insets, magnified views of the SG boundary. Red arrowheads in N,
731 N'', O and O'', high myosin intensity at the SG boudary in control and *smog* null [mild]
732 embryos. Cyan arrowheads in P and P'', low myosin signals at the SG boundary in the
733 *smog* null [severe] embryo. (Q) Circularity of the SG placode boundary. An example of a
734 WT SG stained for E-Cad (magenta) and sqh-GFP (green) with the SG boundary (red
735 line) and the boundaries one cell row outside (gray line) and inside (blue line) the SG
736 boundary. (R) Quantification of circularity of the SG, outer, and inner boundaries.
737 Asterisks, invagination pit. n=5 SGs for each genotype. ns, non-significant; *p≤0.05;
738 **p≤0.01; ***p≤0.001 (Welch's t-test).
739
740 **Figure 5. Smog is required for maintaining epithelial integrity and the microtubule**
741 **networks.** (A-D') Confocal images of stage 11 embryos stained for E-Cad (green in A,
742 B), Crb (green in C, D) and CrebA (magenta). (A'-D') Magnified view of the white boxed
743 region in A-D. Arrowheads in B' and D', E-Cad (B') and Crb (D') signals are absent in
744 regions of the epidermis in *smog* mutants. (E) E-Cad (magenta) and Gap43-mCh
745 (green) signals in the epidermis in the *smog* null [severe] embryo. The cell membrane is
746 intact (cyan arrowheads in E'') in regions where E-Cad signals are absent (yellow
747 arrowheads in E'). (F-K) E-Cad (F-H) and Crb (I-K) signals in SGs in WT (F, I), *smog*
748 null [mild] (G, J), and *smog* null [severe] (H, K) embryos. Insets, magnified view of
749 yellow boxed region in the SG. Arrowheads, gaps in E-Cad or Crb signals. (L-O)
750 Quantification of the number of gaps in E-Cad (L) and Crb (N) signals and the ratio of
751 gap length to total junctional length for E-Cad (M) and Crb (O). n=5 SGs, 50 cells per
752 genotype. ns, non-significant; *p≤0.05; **p≤0.01 (Mann-Whitney U test). (P-W) Ace-tub
753 (P-S) and Tyr-tub (T-W) signals in the SG and the surrounding epithelia. Red dotted
754 lines, SG boundary. (X, Y) Quantification of the ratio of Ace-tub (X) and Tyr-tub (Y)
755 intensity in SG cells to the intensity in cells outside the SG placode. n=5 SGs for each
756 genotype. *p≤0.05; **p≤0.01 (Mann-Whitney U test). Asterisks, invagination pit; Pound
757 sign, dividing cells.
758

759 **Figure 6. Smog is required for maintaining cortical actin networks during SG**
760 **invagination.** (A-B’’’) Rok-GFP (green) and E-Cad (magenta) in stage 11 SGs in
761 control (A-A’’’) and *smog* null [severe] (B-B’’’) embryos. (A’-B’’) Higher magnification of
762 the white boxed regions in A and B. (A’’’, B’’’) x-z sections across the yellow lines in A
763 and B. Red arrowheads, normal Rok-GFP signals accumulated in the medioapical
764 region of control SG cells. White arrowheads, blebs in SG cells in *smog* mutants
765 enriched with Rok-GFP signals. (C-J) SGs stained for phalloidin (C-F) and Dia (G-J).
766 Compared to strong phalloidin and Dia signals in WT (red arrowheads in C, G),
767 phalloidin and Dia levels are reduced in *smog* and *fog* mutants (cyan arrowheads in D-
768 F, yellow arrowheads in H-J). (K) Quantification of total Dia intensity in the SG placode.
769 n=5 SGs for control and *smog* null [mild], n=4 SGs for *smog* null [severe], n=6 SGs for
770 *fog* null. *$p \leq 0.05$; **$p \leq 0.01$ (Mann-Whitney U test). (L-N’’) Rok-GFP (green) and E-Cad
771 (magenta) in *chic* RNAi in the wild-type (L-L’’), *smog* null [mild] (M-M’’), and *chic* RNAi in
772 *smog* mutant background (N-N’’). (L’-N’’) Higher magnification of the white boxed
773 regions in L-N. Red arrowheads in L’, L’’, M’, and M’’, normal Rok-GFP signals in *chic*
774 RNAi and smog null [mild] SGs. White arrowheads in N’ and N’’, membrane blebs with
775 enriched Rok-GFP signals in *smog* null [mild] SG cells with *chic* RNAi. Asterisks,
776 invagination pit.
777
778 **Figure 7. A proposed model for roles of Smog during epithelial tube formation.**
779 During SG invagination, Smog responds to Fog signal to promote Rok accumulation
780 and medioapical myosin formation to control apical constriction (red arrows).
781 Independent of Fog (and responding to an as-yet-unknown ligand X), Smog regulates
782 epithelial integrity by regulating junctional and the supracellular myosin pools, the
783 microtubule networks, and key apical/junctional components (gray arrows). Smog is
784 also required for cortical actin organization during SG invagination, through regulating
785 Dia levels (gray arrows). Different ligands may recruit specific G proteins and RhoGEFs
786 to activate distinct downstream effectors.
787

References

Abreu-Blanco, M. T., Verboon, J. M. and Parkhurst, S. M. (2014). Coordination of Rho Family GTPase Activities to Orchestrate Cytoskeleton Responses during Cell Wound Repair. *Current Biology* **24**, 144–155.

Afshar, K., Stuart, B. and Wasserman, S. A. (2000). Functional analysis of the Drosophila diaphanous FH protein in early embryonic development. *Development (Cambridge, England)* **127**, 1887–97.

Andrew, D. J. and Ewald, A. J. (2010). Morphogenesis of epithelial tubes: Insights into tube formation, elongation, and elaboration. *Developmental Biology* **341**, 34–55.

Aoki, K., Maeda, F., Nagasako, T., Mochizuki, Y., Uchida, S. and Ikenouchi, J. (2016). A RhoA and Rnd3 cycle regulates actin reassembly during membrane blebbing. *Proceedings of the National Academy of Sciences* **113**, E1863–E1871.

Barrett, K., Leptin, M. and Settleman, J. (1997). The Rho GTPase and a Putative RhoGEF Mediate a Signaling Pathway for the Cell Shape Changes in Drosophila Gastrulation. *Cell* **91**, 905–915.

Benton, M. A., Frey, N., Nunes da Fonseca, R., von Levetzow, C., Stappert, D., Hakeemi, M. S., Conrads, K. H., Pechmann, M., Panfilio, K. A., Lynch, J. A., et al. (2019). Fog signaling has diverse roles in epithelial morphogenesis in insects. *eLife* **8**, e47346.

Blanchard, G. B., Murugesu, S., Adams, R. J., Martinez-Arias, A. and Gorfinkiel, N. (2010). Cytoskeletal dynamics and supracellular organisation of cell shape fluctuations during dorsal closure. *Development* **137**, 2743–2752.

Booth, A. J. R., Blanchard, G. B., Adams, R. J. and Röper, K. (2014). A Dynamic Microtubule Cytoskeleton Directs Medial Actomyosin Function during Tube Formation. *Developmental Cell* **29**, 562–576.

Charras, G. T. (2008). A short history of blebbing. *Journal of Microscopy* **231**, 466–478.

Charras, G. T., Yarrow, J. C., Horton, M. A., Mahadevan, L. and Mitchison, T. J. (2005). Non-equilibration of hydrostatic pressure in blebbing cells. *Nature* **435**, 365–369.

Chung, S., Hanlon, C. D. and Andrew, D. J. (2014). Building and specializing epithelial tubular organs: the Drosophila salivary gland as a model system for

819 revealing how epithelial organs are specified, form and specialize. *WIREs Dev Biol*
820 **3**, 281–300.
821 **Chung, S., Kim, S. and Andrew, D. J.** (2017). Uncoupling apical constriction from
822 tissue invagination. *eLife* **6**, e22235.
823 **Cooley, L., Verheyen, E. and Ayers, K.** (1992). chickadee encodes a profilin required
824 for intercellular cytoplasm transport during Drosophila oogenesis. *Cell* **69**, 173–184.
825 **Costa, M., Wilson, E. T. and Wieschaus, E.** (1994). A putative cell signal encoded by
826 the folded gastrulation gene coordinates cell shape changes during Drosophila
827 gastrulation. *Cell* **76**, 1075–1089.
828 **Dawes-Hoang, R. E., Parmar, K. M., Christiansen, A. E., Phelps, C. B., Brand, A. H.**
829 **and Wieschaus, E. F.** (2005). *folded gastrulation* , cell shape change and the
830 control of myosin localization. *Development* **132**, 4165–4178.
831 **Fox, D. T. and Peifer, M.** (2007). Abelson kinase (Abl) and RhoGEF2 regulate actin
832 organization during cell constriction in *Drosophila*. *Development* **134**, 567–578.
833 **Garcia De Las Bayonas, A., Philippe, J. M., Lellouch, A. C. and Lecuit, T.** (2019).
834 Distinct RhoGEFs Activate Apical and Junctional Contractility under Control of G
835 Proteins during Epithelial Morphogenesis. *Current Biology* **29**, 3370-3385.e7.
836 **Girdler, G. C. and Röper, K.** (2014). Controlling cell shape changes during salivary
837 gland tube formation in Drosophila. *Seminars in Cell & Developmental Biology* **31**,
838 74–81.
839 **Goode, B. L. and Eck, M. J.** (2007). Mechanism and Function of Formins in the Control
840 of Actin Assembly. *Annual Review of Biochemistry* **76**, 593–627.
841 **Gorfinkiel, N. and Blanchard, G. B.** (2011). Dynamics of actomyosin contractile
842 activity during epithelial morphogenesis. *Current Opinion in Cell Biology* **23**, 531–
843 539.
844 **Guglielmi, G., Barry, J. D., Huber, W. and de Renzis, S.** (2015). An Optogenetic
845 Method to Modulate Cell Contractility during Tissue Morphogenesis. *Developmental*
846 *cell* **35**, 646–660.
847 **Häcker, U. and Perrimon, N.** (1998). *DRhoGEF2* encodes a member of the Dbl family
848 of oncogenes and controls cell shape changes during gastrulation in *Drosophila*.
849 *Genes & Development* **12**, 274–284.

850 **Henderson, K. D. and Andrew, D. J.** (2000). Regulation and Function of Scr, exd, and
851 hth in the Drosophila Salivary Gland. *Developmental Biology* **217**, 362–374.
852 **Homem, C. C. F. and Peifer, M.** (2008). Diaphanous regulates myosin and adherens
853 junctions to control cell contractility and protrusive behavior during morphogenesis.
854 *Development* **135**, 1005–1018.
855 **Izquierdo, E., Quinkler, T. and de Renzis, S.** (2018). Guided morphogenesis through
856 optogenetic activation of Rho signalling during early Drosophila embryogenesis.
857 *Nature Communications* **9**, 2366.
858 **Jha, A., van Zanten, T. S., Philippe, J.-M., Mayor, S. and Lecuit, T.** (2018).
859 Quantitative Control of GPCR Organization and Signaling by Endocytosis in
860 Epithelial Morphogenesis. *Current Biology* **28**, 1570-1584.e6.
861 **Jodoin, J. N., Coravos, J. S., Chanet, S., Vasquez, C. G., Tworoger, M., Kingston,**
862 **E. R., Perkins, L. A., Perrimon, N. and Martin, A. C.** (2015). Stable Force Balance
863 between Epithelial Cells Arises from F-Actin Turnover. *Developmental Cell* **35**, 685–
864 697.
865 **Kanesaki, T., Hirose, S., Grosshans, J. and Fuse, N.** (2013). Heterotrimeric G protein
866 signaling governs the cortical stability during apical constriction in Drosophila
867 gastrulation. *Mechanisms of Development* **130**, 132–142.
868 **Kerridge, S., Munjal, A., Philippe, J.-M., Jha, A., de las Bayonas, A. G., Saurin, A.**
869 **J. and Lecuit, T.** (2016). Modular activation of Rho1 by GPCR signalling imparts
870 polarized myosin II activation during morphogenesis. *Nature Cell Biology* **18**, 261–
871 270.
872 **Kim, H. Y., Varner, V. D. and Nelson, C. M.** (2013). Apical constriction initiates new
873 bud formation during monopodial branching of the embryonic chicken lung.
874 *Development* **140**, 3146–3155.
875 **Knirr, S., Azpiazu, N. and Frasch, M.** (1999). The role of the NK-homeobox gene
876 slouch (S59) in somatic muscle patterning. *Development (Cambridge, England)* **126**,
877 4525–35.
878 **Ko, C. S., Tserunyan, V. and Martin, A. C.** (2019). Microtubules promote intercellular
879 contractile force transmission during tissue folding. *Journal of Cell Biology* **218**,
880 2726–2742.

881 **Kölsch, V., Seher, T., Fernandez-Ballester, G. J., Serrano, L. and Leptin, M.** (2007).
882 Control of *Drosophila* Gastrulation by Apical Localization of Adherens Junctions and
883 RhoGEF2. *Science* **315**, 384–386.
884 **Le, T. P. and Chung, S.** (2021). Regulation of apical constriction via microtubule- and
885 Rab11-dependent apical transport during tissue invagination. *Molecular Biology of*
886 *the Cell* **32**, 1033–1047.
887 **le Droguen, P.-M., Claret, S., Guichet, A. and Brodu, V.** (2015). Microtubule-
888 dependent apical restriction of recycling endosomes sustains adherens junctions
889 during morphogenesis of the *Drosophila* tracheal system. *Development* **142**, 363–
890 374.
891 **Levayer, R. and Lecuit, T.** (2012). Biomechanical regulation of contractility: spatial
892 control and dynamics. *Trends in cell biology* **22**, 61–81.
893 **Lord, S. J., Velle, K. B., Mullins, R. D. and Fritz-Laylin, L. K.** (2020). SuperPlots:
894 Communicating reproducibility and variability in cell biology. *Journal of Cell Biology*
895 **219**, e202001064.
896 **Lubarsky, B. and Krasnow, M. A.** (2003). Tube morphogenesis: making and shaping
897 biological tubes. *Cell* **112**, 19–28.
898 **Manning, A. J. and Rogers, S. L.** (2014). The Fog signaling pathway: Insights into
899 signaling in morphogenesis. *Developmental Biology* **394**, 6–14.
900 **Manning, A. J., Peters, K. A., Peifer, M. and Rogers, S. L.** (2013). Regulation of
901 Epithelial Morphogenesis by the G Protein–Coupled Receptor Mist and Its Ligand
902 Fog. *Science Signaling* **6**, ra98.
903 **Martin, A. C. and Goldstein, B.** (2014). Apical constriction: themes and variations on a
904 cellular mechanism driving morphogenesis. *Development* **141**, 1987–1998.
905 **Martin, A. C., Kaschube, M. and Wieschaus, E. F.** (2009). Pulsed contractions of an
906 actin–myosin network drive apical constriction. *Nature* **457**, 495–499.
907 **Martin, A. C., Gelbart, M., Fernandez-Gonzalez, R., Kaschube, M. and Wieschaus,**
908 **E. F.** (2010). Integration of contractile forces during tissue invagination. *Journal of*
909 *Cell Biology* **188**, 735–749.
910

911 **Mason, F. M., Tworoger, M. and Martin, A. C.** (2013). Apical domain polarization
912 localizes actin–myosin activity to drive ratchet-like apical constriction. *Nature Cell*
913 *Biology* **15**, 926–936.
914 **Massarwa, R., Schejter, E. D. and Shilo, B.-Z.** (2009). Apical Secretion in Epithelial
915 Tubes of the Drosophila Embryo Is Directed by the Formin-Family Protein
916 Diaphanous. *Developmental Cell* **16**, 877–888.
917 **Munjal, A. and Lecuit, T.** (2014). Actomyosin networks and tissue morphogenesis.
918 *Development (Cambridge, England)* **141**, 1789–93.
919 **Myat, M. M. and Andrew, D. J.** (2000). Organ shape in the Drosophila salivary gland is
920 controlled by regulated, sequential internalization of the primordia. *Development*
921 *(Cambridge, England)* **127**, 679–91.
922 **Nikolaidou, K. K. and Barrett, K.** (2004). A Rho GTPase Signaling Pathway Is Used
923 Reiteratively in Epithelial Folding and Potentially Selects the Outcome of Rho
924 Activation. *Current Biology* **14**, 1822–1826.
925 **Parks, S. and Wieschaus, E.** (1991). The drosophila gastrulation gene concertina
926 encodes a Gα-like protein. *Cell* **64**, 447–458.
927 **Plageman, T. F., Chauhan, B. K., Yang, C., Jaudon, F., Shang, X., Zheng, Y., Lou,**
928 **M., Debant, A., Hildebrand, J. D. and Lang, R. A.** (2011). A Trio-RhoA-Shroom3
929 pathway is required for apical constriction and epithelial invagination. *Development*
930 **138**, 5177–5188.
931 **Rao, M. V. and Zaidel-Bar, R.** (2016). Formin-mediated actin polymerization at cell–cell
932 junctions stabilizes E-cadherin and maintains monolayer integrity during wound
933 repair. *Molecular Biology of the Cell* **27**, 2844–2856.
934 **Romero, S., le Clainche, C., Didry, D., Egile, C., Pantaloni, D. and Carlier, M.-F.**
935 (2004). Formin Is a Processive Motor that Requires Profilin to Accelerate Actin
936 Assembly and Associated ATP Hydrolysis. *Cell* **119**, 419–429.
937 **Röper, K.** (2012). Anisotropy of Crumbs and aPKC Drives Myosin Cable Assembly
938 during Tube Formation. *Developmental Cell* **23**, 939–953.
939 **Rousso, T., Shewan, A. M., Mostov, K. E., Schejter, E. D. and Shilo, B.-Z.** (2013).
940 Apical targeting of the formin Diaphanous in Drosophila tubular epithelia. *eLife* **2**, 1–
941 19.

942 **Royou, A., Field, C., Sisson, J. C., Sullivan, W. and Karess, R.** (2004). Reassessing
943 the Role and Dynamics of Nonmuscle Myosin II during Furrow Formation in Early
944 *Drosophila* Embryos. *Molecular Biology of the Cell* **15**, 838–850.
945 **Sanchez-Corrales, Y. E., Blanchard, G. B. and Röper, K.** (2018). Radially patterned
946 cell behaviours during tube budding from an epithelium. *eLife* **7**, e35717.
947 **Shewan, A. M., Maddugoda, M., Kraemer, A., Stehbens, S. J., Verma, S., Kovacs,**
948 **E. M. and Yap, A. S.** (2005). Myosin 2 Is a Key Rho Kinase Target Necessary for
949 the Local Concentration of E-Cadherin at Cell–Cell Contacts. *Molecular Biology of*
950 *the Cell* **16**, 4531–4542.
951 **Sidor, C., Stevens, T. J., Jin, L., Boulanger, J. and Röper, K.** (2020). Rho-Kinase
952 Planar Polarization at Tissue Boundaries Depends on Phospho-regulation of
953 Membrane Residence Time. *Developmental Cell* **52**, 364-378.e7.
954 **Sweeton, D., Parks, S., Costa, M. and Wieschaus, E.** (1991). Gastrulation in
955 Drosophila: the formation of the ventral furrow and posterior midgut invaginations.
956 *Development (Cambridge, England)* **112**, 775–89.
957 **Vázquez-Victorio, G., González-Espinosa, C., Espinosa-Riquer, Z. P. and Macías-**
958 **Silva, M.** (2016). GPCRs and actin–cytoskeleton dynamics. *Methods in Cell Biology*
959 **132**, 165–188.
960 **Weng, M. and Wieschaus, E.** (2016). Myosin-dependent remodeling of adherens
961 junctions protects junctions from Snail-dependent disassembly. *Journal of Cell*
962 *Biology* **212**, 219–229.
963 **Westermann, S. and Weber, K.** (2003). Post-translational modifications regulate
964 microtubule function. *Nature Reviews Molecular Cell Biology* **4**, 938–948.
965 **Zweifel, M. E. and Courtemanche, N.** (2020). Profilin's Affinity for Formin Regulates
966 the Availability of Filament Ends for Actin Monomer Binding. *Journal of Molecular*
967 *Biology* **432**, 166688.
968

Figure 1.

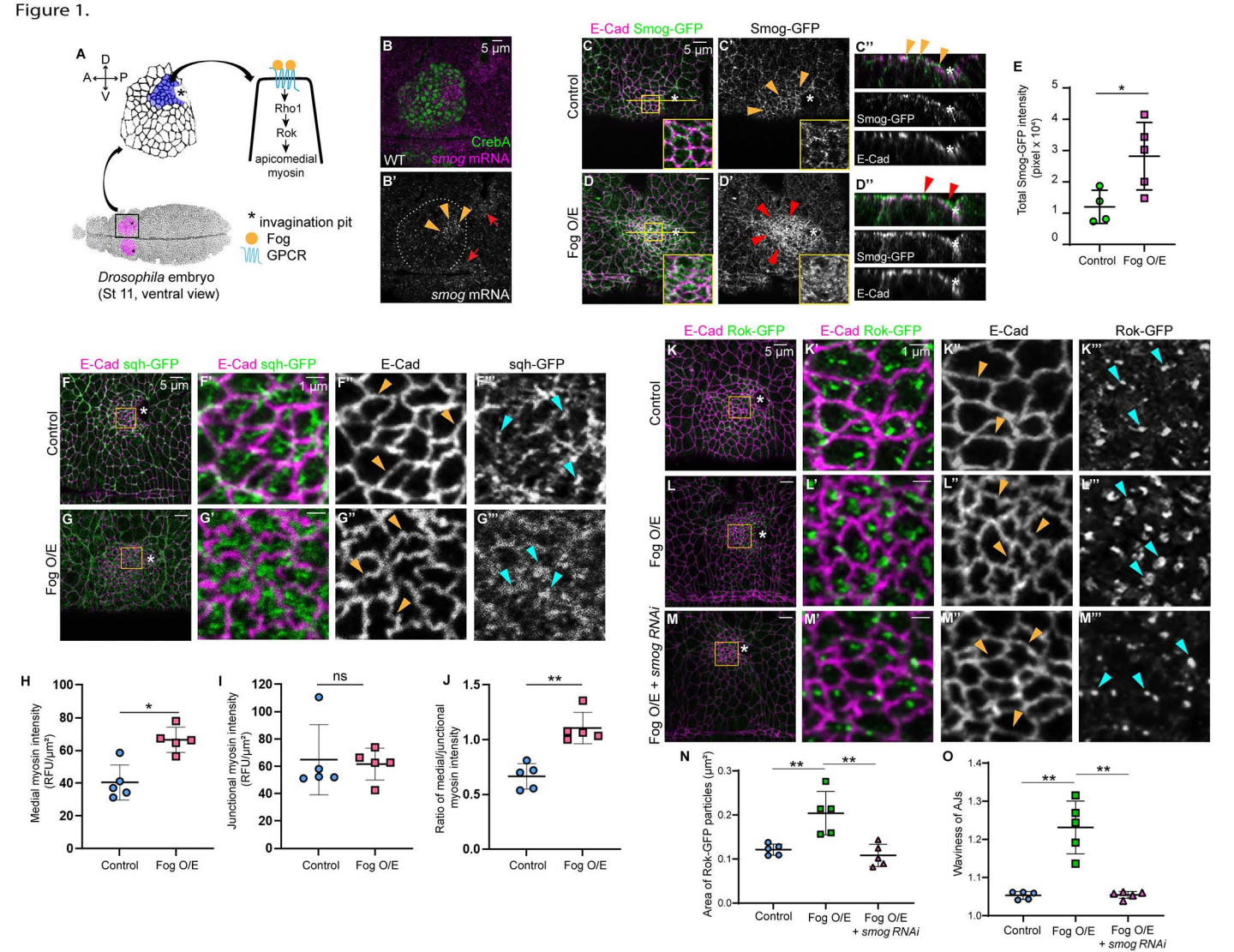
A
D
A
P
V
Rho1
Rok
apicomedial myosin
* invagination pit
Fog
GPCR
Drosophila embryo
(St 11, ventral view)
B
5 µm
CrebA
WT
smog mRNA
B'
smog mRNA
E-Cad Smog-GFP
Smog-GFP
Control
Fog O/E
C
C'
C''
D
D'
D''
Smog-GFP
E-Cad
E
Total Smog-GFP intensity (pixel x 10⁴)
Control
Fog O/E
E-Cad sqh-GFP
E-Cad
sqh-GFP
F
F'
F''
F'''
G
G'
G''
G'''
1 µm
H
Medial myosin intensity (RFU/µm²)
I
Junctional myosin intensity (RFU/µm²)
ns
J
Ratio of medial/junctional myosin intensity
E-Cad Rok-GFP
Rok-GFP
K
K'
K''
K'''
L
L'
L''
L'''
M
M'
M''
M'''
Fog O/E + smog RNAi
N
Area of Rok-GFP particles (µm²)
Fog O/E + smog RNAi
O
Waviness of AJs

Figure 2.

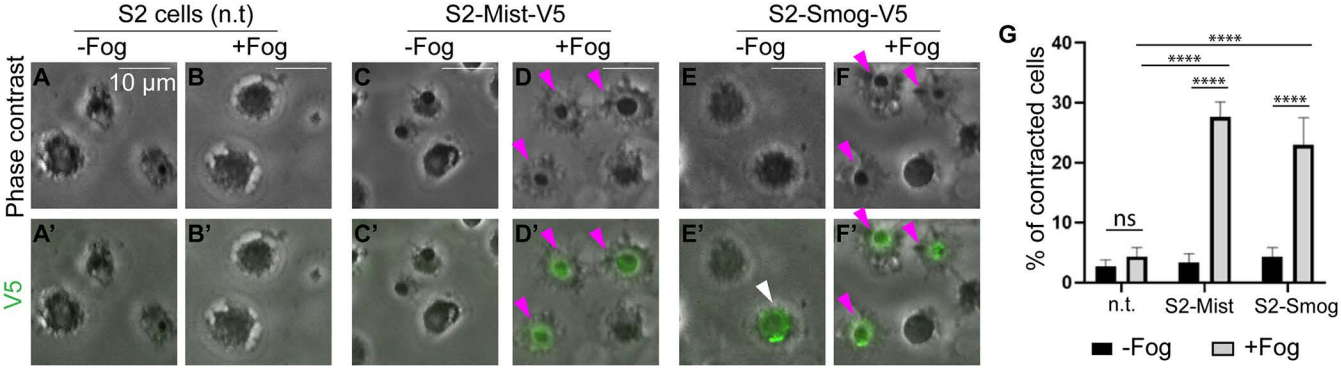
S2 cells (n.t)
S2-Mist-V5
S2-Smog-V5
-Fog
+Fog
Phase contrast
V5
10 µm
A
B
C
D
E
F
A'
B'
C'
D'
E'
F'
G
% of contracted cells
40
30
20
10
0
ns
****
n.t.
S2-Mist
S2-Smog
-Fog
+Fog

Figure 3.

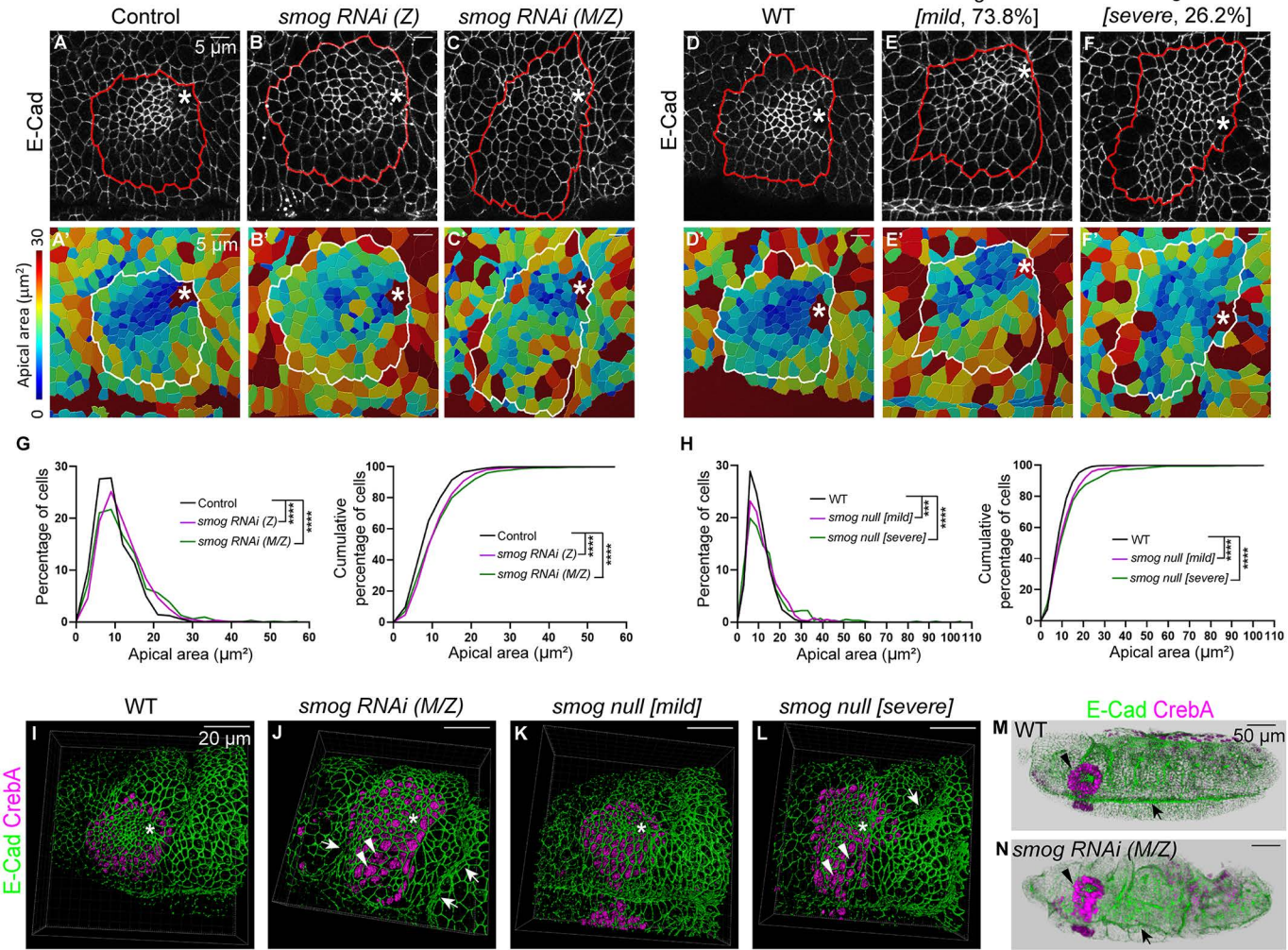
Control
smog RNAi (Z)
smog RNAi (M/Z)
WT
smog null [mild, 73.8%]
smog null [severe, 26.2%]
E-Cad
5 µm
Apical area (µm²)
30
0
G
H
Percentage of cells
Cumulative percentage of cells
Apical area (µm²)
Control
smog RNAi (Z)
smog RNAi (M/Z)
WT
smog null [mild]
smog null [severe]
***
****
WT
smog RNAi (M/Z)
smog null [mild]
smog null [severe]
E-Cad CrebA
20 µm
50 µm
M
N

Figure 4.

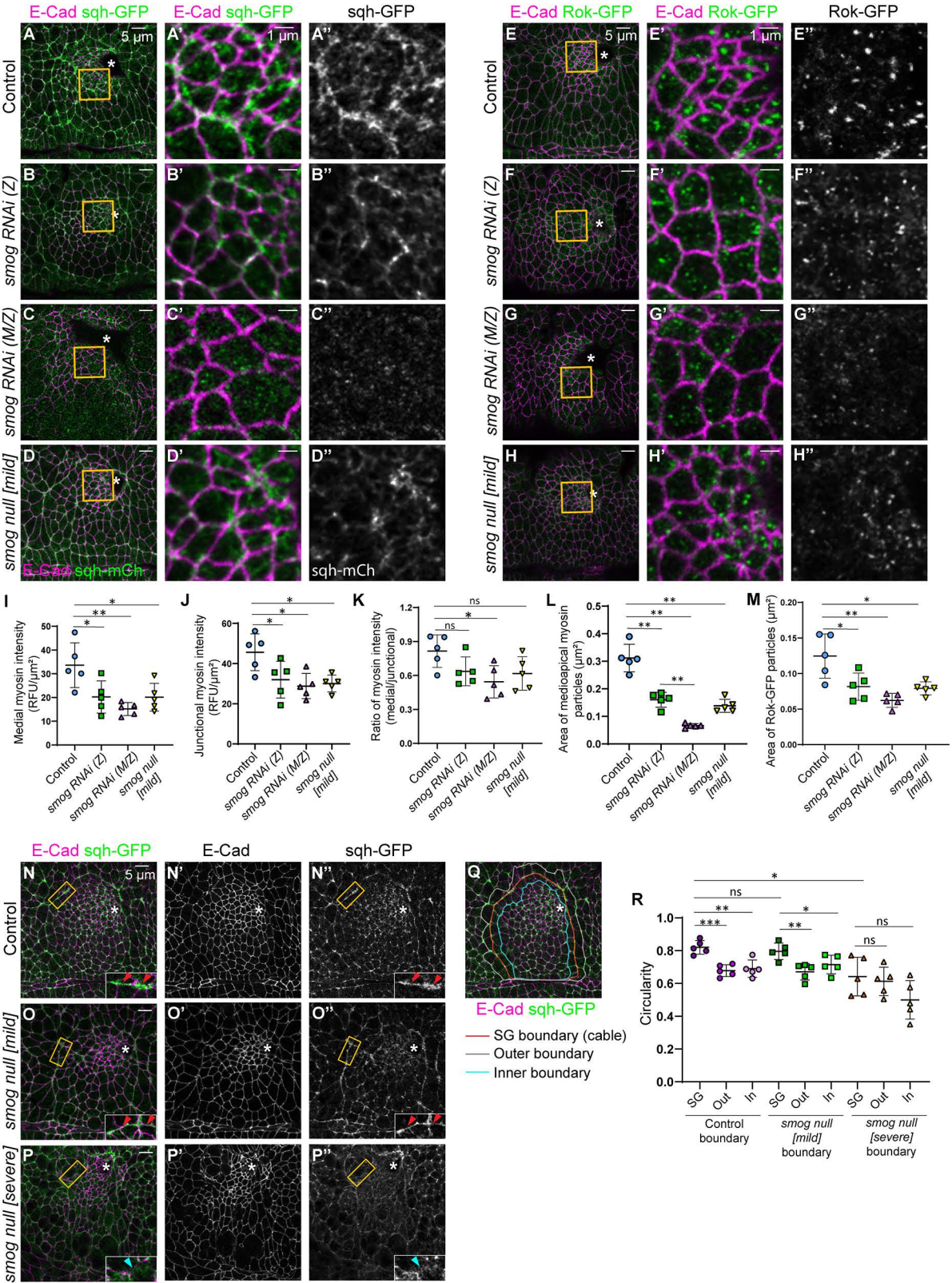
E-Cad sqh-GFP
E-Cad sqh-GFP
sqh-GFP
E-Cad Rok-GFP
E-Cad Rok-GFP
Rok-GFP
Control
smog RNAi (Z)
smog RNAi (M/Z)
smog null [mild]
5 µm
1 µm
E-Cad sqh-mCh
sqh-mCh
Medial myosin intensity (RFU/µm²)
Junctional myosin intensity (RFU/µm²)
Ratio of myosin intensity (medial/junctional)
Area of medioapical myosin particles (µm²)
Area of Rok-GFP particles (µm²)
E-Cad
smog null [severe]
E-Cad sqh-GFP
SG boundary (cable)
Outer boundary
Inner boundary
Circularity
SG
Out
In
Control boundary
smog null [mild] boundary
smog null [severe] boundary

Figure 5.

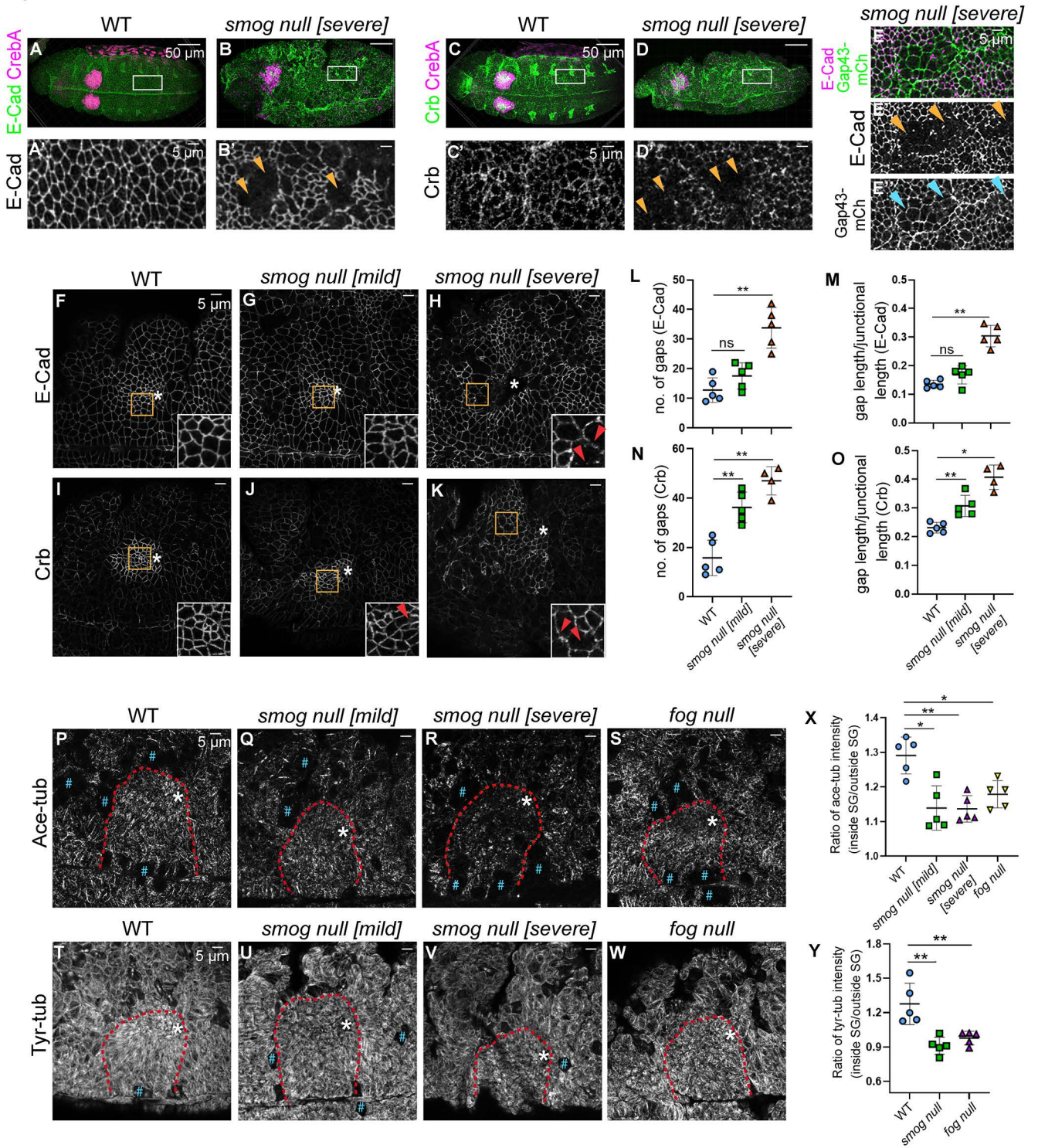
WT
smog null [severe]
E-Cad CrebA
E-Cad
50 µm
5 µm
Crb CrebA
Crb
E-Cad Gap43-mCh
Gap43-mCh
smog null [mild]
ns
no. of gaps (E-Cad)
gap length/junctional length (E-Cad)
no. of gaps (Crb)
gap length/junctional length (Crb)
smog null [severe]
Ace-tub
Tyr-tub
fog null
Ratio of ace-tub intensity (inside SG/outside SG)
Ratio of tyr-tub intensity (inside SG/outside SG)
smog null

Figure 6.

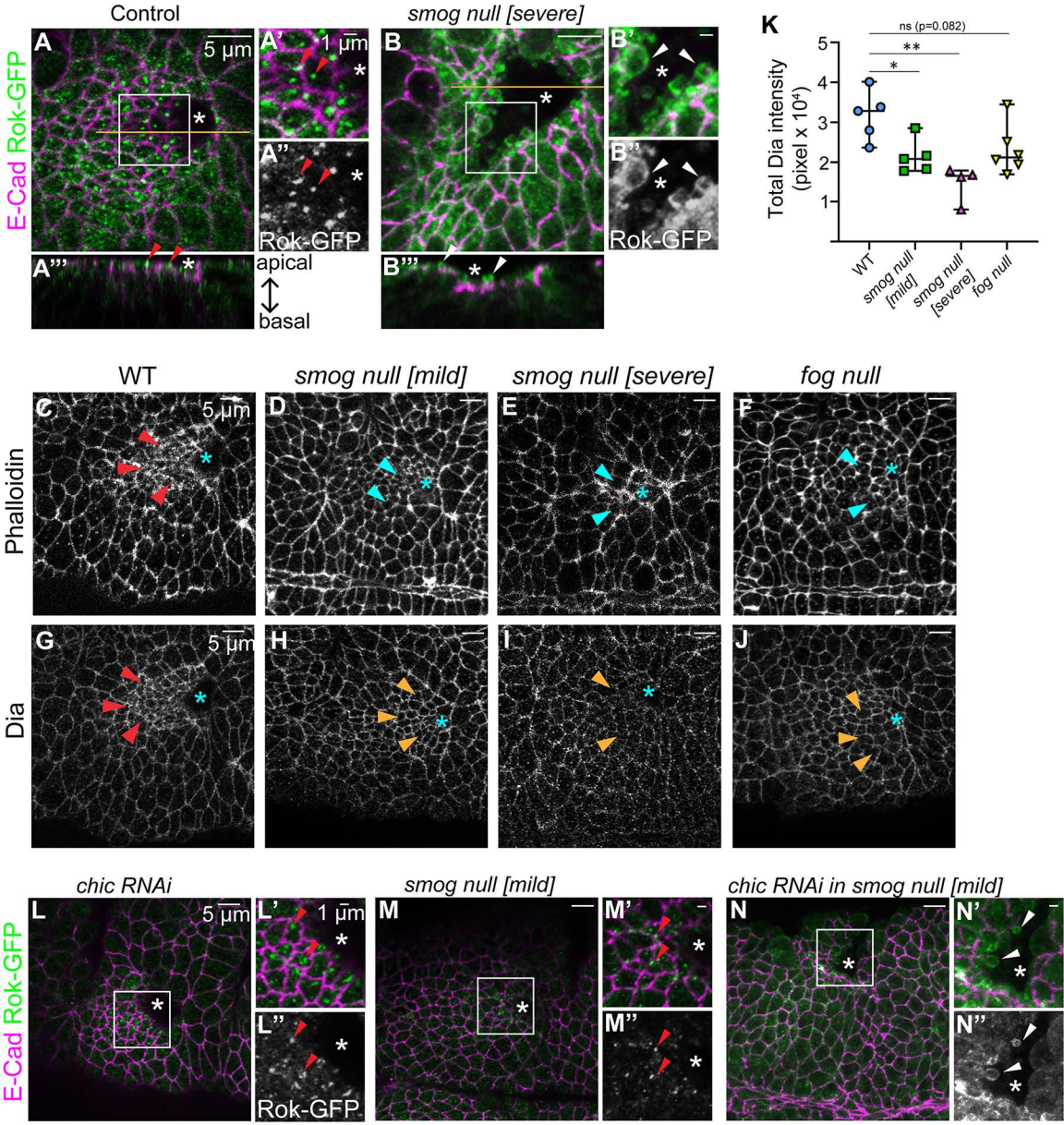
Control
smog null [severe]
E-Cad Rok-GFP
A
5 µm
A'
1 µm
A''
Rok-GFP
A'''
apical
basal
B
B'
B''
Rok-GFP
B'''
K
ns (p=0.082)
**
*
Total Dia intensity (pixel x 10⁴)
WT
smog null [mild]
smog null [severe]
fog null
WT
smog null [mild]
smog null [severe]
fog null
Phalloidin
C
D
E
F
Dia
G
H
I
J
chic RNAi
smog null [mild]
chic RNAi in smog null [mild]
L
L'
L''
M
M'
M''
N
N'
N''

Figure 7.

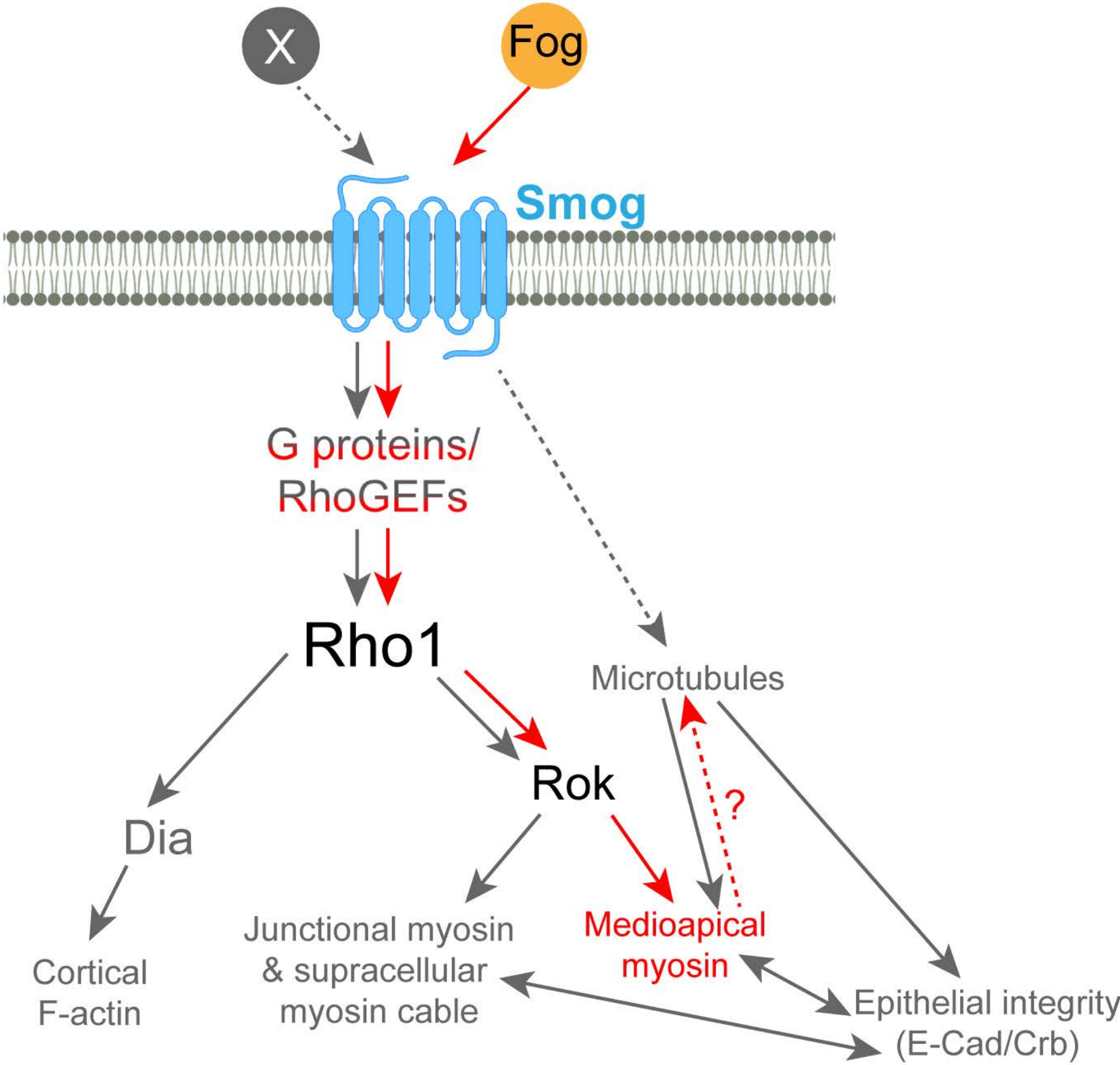
X
Fog
Smog
G proteins/
RhoGEFs
Rho1
Microtubules
Rok
?
Dia
Cortical
F-actin
Junctional myosin
& supracellular
myosin cable
Medioapical
myosin
Epithelial integrity
(E-Cad/Crb)